Energy & Environmental Science

ROYAL SOCIETY OF CHEMISTRY

PAPER

View Article Online
View Journal | View Issue

Cite this: *Energy Environ. Sci.*, 2025, **18**, 3376

Record thermoelectric figure of merit in $Bi_{1-x}Sb_x$ achieved by 1-D Landau level quantization†

Bin He,[a] Xiaolong Feng,[a] Dong Chen,[a] Federico M. Serrano-Sanchez,[a] Mohamed Nawwar,[b] Haihua Hu,[a] Urlich Burkhardt,[a] Berit H. Goodge,[a] Claudia Felser,*[a] Joseph P. Heremans *[bcd] and Yu Pan *[ae]

Received 15th January 2025,
Accepted 21st February 2025

DOI: 10.1039/d5ee00253b

rsc.li/ees

Landau-level quantization confines electrons to a one-dimensional motion, generating a nearly δ-like energy distribution of the density of states that enhances the Seebeck coefficient and produces a high zT in an otherwise three-dimensional system. This mechanism is shown experimentally to create a record figure of merit of zT = 2.6 ± 0.26 at 100 K in an optimally n-type-doped single-crystalline $Bi_{88}Sb_{12}$ topological insulator, in a magnetic field of 0.4 T that is easily reached with permanent magnets. The result is confirmed to be reproducible on two samples and using two different measurement methods. The alloy is unique in that Landau levels are still distinct at 100 K. Quantization more than doubles the Seebeck coefficient and enhances the zT by a factor of 5 over the zero-field value, confirming the significant role that the quantum effect can play in thermoelectric research, especially in low-temperature cooling applications.

Broader context

As environmental protection receives increasing attention, compressor-free techniques have gained appeal, particularly given the detrimental effects of chlorine-based cryogens on atmospheric ozone. The development of solid-state cooling devices utilizing thermoelectric materials presents an effective method for achieving cooling without compressors, because these materials can directly convert electricity into a temperature gradient. While significant advancements have been made in room temperature thermoelectric cooling devices, those designed to operate between 200 K and liquid nitrogen temperatures remain lacking. This study leverages a combination of quantum mechanics and thermoelectric principles to achieve a high figure of merit within the temperature range of 100 K to 200 K. By implementing Landau levels, we achieved synergistic optimization of transport properties that is typically attainable only in low-dimensional materials. Our findings hold great potential for application in cryogenic systems that do not rely on liquid helium.

Main

Thermoelectric energy conversion is an all-solid-state power generation and cooling/refrigeration technology that is green-house-gas free, maintenance free, vibration free, and has a very high power density. However, the thermal efficiency is limited by irreversible thermodynamic losses characterized by the thermoelectric figure of merit $zT = S^2T/\rho\kappa$, where S is the Seebeck coefficient, T is the average temperature, ρ is the resistivity, and κ is the thermal conductivity.[1] Thirty years ago, Hicks and Dresselhaus predicted that the one-dimensional (1-D) quantization of electron motion greatly enhanced zT by enhancing S,[2] since the density of states of 1-D electrons is an almost δ-shaped function of energy,[3] in contrast to that of three-dimensional (3-D) electrons. The present paper reports the successful embodiment of the 1-D quantum enhancement of zT in a 3-D solid using Landau-level (LL) quantization, which confines electron motion to 1-D in the direction parallel to the applied magnetic field B, while quantizing the motion in cyclotron orbits in the plane perpendicular to it. The conversion from the classic 3-D transport into 1-D Landau levels by a magnetic field is briefly summarized in Fig. 1(a). Based on this principle, we obtained an experimental zT of 2.6 ± 0.26 at 100 K and 0.4 T, five times higher than the zero-field value and comparable to those of the best performance high-temperature thermoelectric materials, in the

[a] *Max Planck Institute for Chemical Physics of Solids, Dresden, 01187, Germany. E-mail: Claudia.Felser@cpfs.mpg.de, yupan2024@cqu.edu.cn*
[b] *Department of Materials Science and Engineering, The Ohio State University, Columbus, OH, 43210, USA. E-mail: Heremans.1@osu.edu*
[c] *Department of Mechanical and Aerospace Engineering, The Ohio State University, Columbus, OH, 43210, USA*
[d] *Department of Physics, The Ohio State University, Columbus, OH, 43210, USA*
[e] *College of Materials Science and Engineering & Center of Quantum Materials & Devices, Chongqing University, Chongqing, 400044, China*

† Electronic supplementary information (ESI) available. See DOI: https://doi.org/10.1039/d5ee00253b

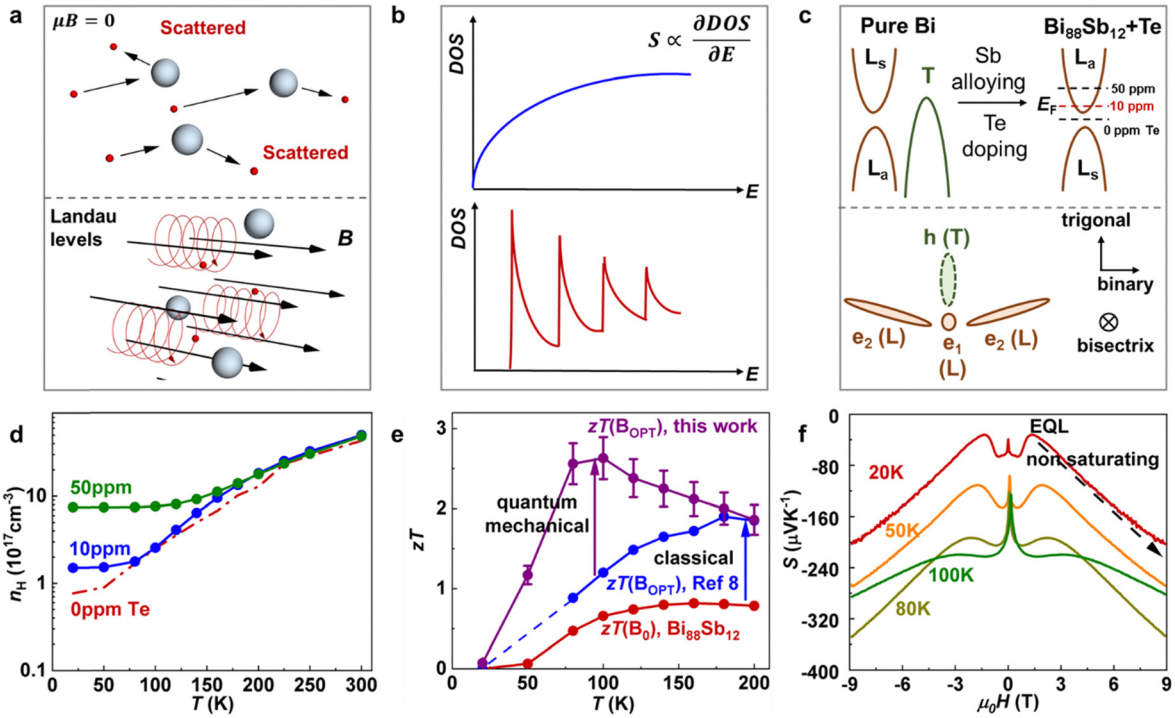

Fig. 1 Landau level quantization enhanced magneto-thermoelectric performance. (a) and (b) Scenario of electrical transport in solids with the corresponding DOS. At zero field, the electrons (red small balls) are constantly scattered. In this case, the DOS $\propto \sqrt{E}$ holds. When a strong field is applied, the electrons are subjected to the Lorentz force and move additionally in the cyclotron motion. The electrons enter the Landau levels at a high field, with the DOS being δ-shaped. (c) Upper: Band structure of pure Bi compared with that of $Bi_{88}Sb_{12}$ with doping. After alloying with Sb, the T-hole band moves far from the Fermi energy, making it possible to remove the multi-carrier effect in Bi. Further doping can effectively move the Fermi energy into the conduction band. Lower: Fermi surface of doped $Bi_{88}Sb_{12}$ viewed from the bisectrix axis, the direction of the applied magnetic field. In this view, the three electron pockets are split into two types, namely, light bisectrix (LBX) and heavy bisectrix (HBX), with the projection being close to a circle and cigar, respectively. The hole Fermi surface locates at the *T* point, which vanishes after alloying with Sb and electron doping. (d) Hall carrier concentrations of different doping level $Bi_{88}Sb_{12}$ samples. (e) Field enhancement of *zT* in $Bi_{88}Sb_{12}$. Without doping, the enhancement is maximized around 200 K, which is dominated by a classical magneto-Seebeck effect.[5] After optimal doping, the Landau quantization creates δ-like DOS that gives a quantum enhancement to the *zT*, mainly happens near 100 K with a much higher amplitude. (f) Non-saturating Seebeck coefficient observed at high field for the 10-ppm doped crystal. The quantum limit shifts to higher fields with an increasing temperature because of a higher carrier concentration.

class of precisely doped single-crystal $Bi_{88}Sb_{12}$, the first topological insulator (TI).[4]

Because *S*, *ρ*, and *κ* are interdependent on each other, the optimization of *zT* has always been a challenge,[6] an approach that synergistically optimizes the three transport parameters has been scarce to date. In the past few decades, the main success of high thermoelectric performance has been achieved at high temperatures (>300 K) with a variety of material engineering techniques,[7] while a high-performance, low-temperature thermoelectric material remains absent except $Bi_{1-x}Sb_x$,[5,8] particularly near the liquid nitrogen temperature.[9] In metal/heavily doped semiconductors, *S* is the energy derivative of the energy-dependent electrical conductivity *σ*(*E*).[10]

$$S = \frac{\pi^2}{3}\frac{k_B}{e}k_B T\left(\frac{\mathrm{d}\ln\sigma(E)}{\mathrm{d}E}\right) \quad (1)$$

Here, *σ*(*E*) is the energy-dependent electrical conductivity, k_B is the Boltzmann constant, and *e* is the elementary charge. Based on eqn (1), Mahan and Sofo proposed that a δ-like distribution of the electronic density of states (δ-DOS) is ideal for high thermoelectric performance with the highest possible *zT* of 14.[11] Early experimental attempts focus on size quantization, for instance, an enhanced Seebeck coefficient is achieved in Bi nanowires,[12] and enhancement in *zT* is observed in Si nanowires[13] due to a reduction of the thermal conductivity. Nevertheless, because the amount of power in a thermoelectric generator or cooler is proportional to the sample volume, a 3-D solid with 1-D transport is highly preferred over nanowires.

LL quantization achieves this and occurs in the $Bi_{1-x}Sb_x$ class of narrow-gap semiconductors at up to 100 K. Note that LLs were originally discovered less than a century ago by observing the Shubnikov–de Haas (SdH) oscillations in the end member of this class, semimetal Bi.[14] In order to realize LL quantization in a $Bi_{88}Sb_{12}$ topological insulator, precise tuning of the Fermi energy into the conduction band is essential. For pristine $Bi_{88}Sb_{12}$, a strong magneto-Seebeck effect and high magneto-*zT* have been realized;[5,8] however, there is an absence of Shubnikov–de Haas (SdH) oscillations even though the mobility is as high as 8×10^5 cm^2 V^{-1} s^{-1} (at 80 K).[5] We, herein, therefore performed optimal Fermi energy tuning in the conduction band by ppm-level Te doping. Owing to the high

mobility and suitable Fermi energy, SdH oscillations starting from a low field (<0.1 T) at 2 K and LL quantization are observed in a single-crystalline Te-doped $Bi_{88}Sb_{12}$ topological insulator. As a consequence, the electron motion transverse to the field is then quantized onto the LLs, developing a δ-DOS (Fig. 1(b)) that meets the Mahan–Sofo criterion[11] and significantly enhances the zT (80 to 160 K). This new approach based on quantum mechanical rather than classical transport greatly improves the zT of $Bi_{88}Sb_{12}$ at fields sufficiently low to be generated by a permanent magnet, which is very desirable in practical applications.

Pure Bi is a classic semimetal with an equal density of electrons and holes.[15] In Bi, electrons and light holes form symmetric bands centered at the *L*-points of the Brillouin zone (BZ), whereas a heavy hole band is populated at the *T*-points.[16] Alloying pure Bi with Sb results in a decrease in the lattice constant, which decreases the energy of the T-hole band and decreases the direct band gap of the *L*-point electrons and holes, eventually inverting these bands and creating direct-gap semiconducting topological insulators for $x > 7\%$.[17,18] Fig. 1(c) shows the band structures of pure Bi and 12% Sb-alloyed $Bi_{88}Sb_{12}$. Ideally, for the pristine $Bi_{88}Sb_{12}$, the Fermi energy locates in the mid-gap. The *L*-point pockets of both are almost mirror images, except for the band inversion and the disappearance of the trivial band at the *T*-point that makes $Bi_{88}Sb_{12}$ a topological insulator.[4] To locate the Fermi energy into the conduction band, n-type doping is necessary. Experimentally, we prepared multiple $Bi_{88}Sb_{12}$ single crystals by the horizontal zone melting technique with different nominal doping levels of 0, 10, and 50 ppm of Te, with the Fermi energies schematically shown as the dashed lines in the upper panel of Fig. 1(c). The actual Te concentrations in the crystal were tested by inductively coupled plasma (ICP) measurement and the results are briefly summarized in Table S1 (ESI†). After doping, the Fermi surface of n-type doped $Bi_{88}Sb_{12}$ viewed into the bisectrix axis is shown in the lower panel of Fig. 1(c). The electron pockets are slightly tilted in the Γ–*L* direction. Viewed along (010), the direction along which the field is applied here, the electron Fermi surface cross-sections fall into two groups: a nearly circular light bisectrix (LBX) and two elliptical anisotropic heavy bisectrices (HBXs).[19,20] The T-hole band is shown as a dashed oval since it is far from the Fermi energy after doping; it does not contribute to transport below about 200 K.

Transport properties are measured along the trigonal direction with the highest mobility. The zero-field transport properties of the three crystals are summarized in Fig. S1 (ESI†). The increased Hall carrier concentrations n_H in Fig. 1(d) confirm that the Fermi energies of the doped samples are shifted toward the conduction band. At 20 K, the n_H increases from 7×10^{16} cm^{-3} in the undoped sample to 7×10^{17} cm^{-3} for the nominal 50-ppm crystal. For all crystals, n_H increases with temperature because of the thermal excitation of the intrinsic carriers. Among the three crystals, the 10-ppm crystal is optimally doped and shows the best zT (details later). A zT-comparison between the pristine and doped $Bi_{88}Sb_{12}$ crystals is summarized in Fig. 1(e). For the 10-ppm crystal, the zT measured at zero field is shown as a red curve, labeled as $zT(B_0)$; the zT measured at optimal field (B_{OPT}, with the highest zT at each temperature) is shown as a purple curve, labeled as $zT(B_{OPT})$. Notably, $zT(B_{OPT})$ is five times higher than $zT(B_0)$ at 100 K. Moreover, we compared the present result to our previous result without LL quantization, as shown by the blue curve. Obviously, there is a great enhancement of the present work compared to our previous report, and the current best zT of 2.6 at 100 K is 2.2 times higher than that of the previously reported result,[8] suggesting the significance of LL quantization in zT enhancement. This high zT also provides the opportunity for thermoelectric device fabrication near liquid nitrogen temperature. At high temperatures above 100 K, the intrinsically excited carriers become dominant in transport and the quantum enhancement gradually vanishes.

Proven as a topological insulator, the quantum enhancement arises from the linear Dirac bands rather than the topological surface states. Predicted by theory,[21] a non-saturating magneto-Seebeck effect is expected with the topological linear bands in the extreme quantum limit (EQL) when all carriers are on the last LL, which is exceptional compared to parabolic bands. This is observed in the present system: Fig. 1(f) reports high-field measurements of the Seebeck coefficient up to 9 T. At temperatures up to 100 K, the high-field thermopower increases linearly with the field, which has been absent in previous reports.[8,22] The large, non-saturating magneto Seebeck effect provides evidence to distinguish this study from the previous ones, and highlights the importance of the quantum mechanical contribution to thermoelectric performance. The EQL increases from 1.2 T to 4.2 T in this sample because n_H increases as well. The peak zT is observed at 100 K but at a field where 2 or 3 LL's are filled. This provides evidence for the quantum LL nature of the zT enhancement. Above 100 K, n_H increases with T (Fig. 1(d)) due to the appearance of thermally excited holes and electrons. This reduces the peak zT, but not dramatically and the zT enhancement persists up to 180 K. Similarly, at $T > 100$ K, the non-saturating Seebeck coefficient vanishes progressively (ESI,† Fig. S2(b)).

Field-dependent thermoelectric transport properties

The magnetic field dependence of S, ρ, and κ with B along the bisectrix direction are given next. The 10-ppm doped sample shows the best thermoelectric performance, as summarized in Fig. 2; the undoped and 50-ppm doped samples are under- and over-doped, respectively (as summarized in Fig. S3 and S5, ESI†). For the 10-ppm crystal, a series of sample characterization studies, including the crystal quality, phase purity, compositional homogeneity, is summarized in the ESI,† Fig. S6–S8, to show its high crystal quality. Additionally, transmission electron microscopy (TEM) measurement was executed to eliminate any possible microstructure and to guarantee the bulk transport behavior. Fig. 2(a) shows the low-temperature SdH oscillations of ρ in the 10-ppm crystal. Below 10 K, they are clearly resolved starting from a very low field (<0.1 T). ρ decreases to a local minimum for $0.1\ T < B < 0.5$ T. At and above 1.2 T, which is shown later to be the EQL for HBX carriers, ρ increases monotonically with B. Oscillations

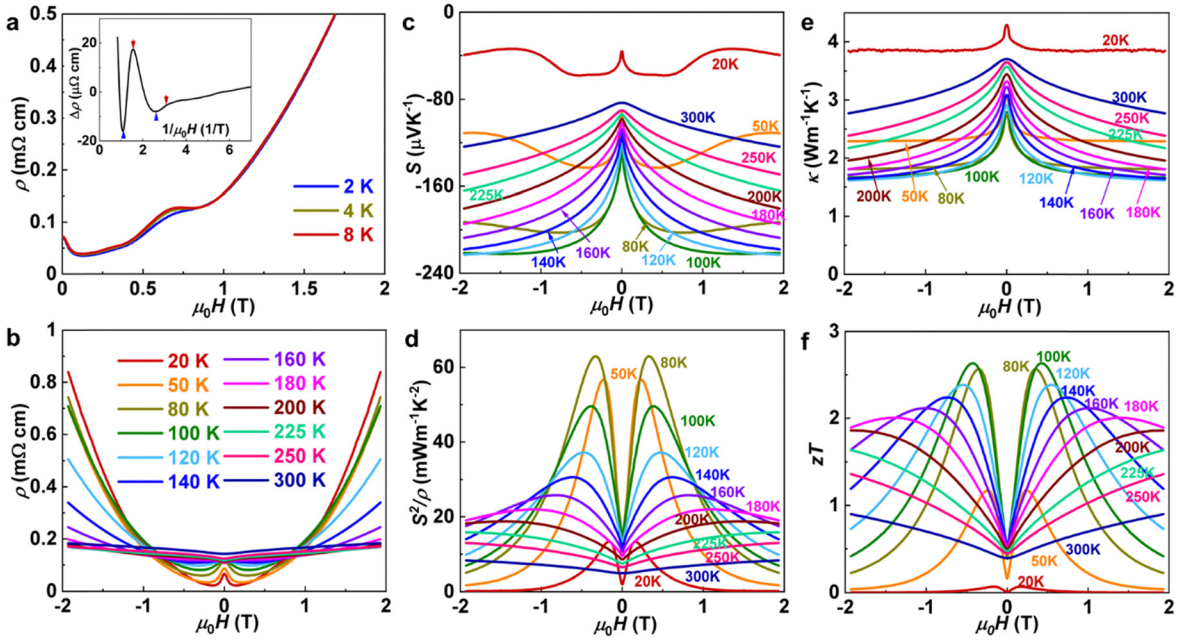

Fig. 2 Transport properties of a 10-ppm Te-doped $Bi_{88}Sb_{12}$ single crystal under a magnetic field. (a) Low-temperature (2–8 K) field dependence of resistivity. A clear SdH effect is observed, from which we resolve the size of the Fermi surface, which is much smaller than that in pure Bi. (b) Higher temperature in-field resistivity. SdH oscillations are still resolved up to 100 K because of a small effective mass and high mobility; they gradually vanish above 100 K. (c) Seebeck responses. An oscillatory signal can be clearly observed below 100 K. Above 100 K, it shows the behavior of a thermally excited semiconductor. (d) Power factor. Due to the negative in-field resistivity, the power factor reaches the maxima at low field and low temperature, with the peak value over 60 mW m^{-1} K^{-2}. (e) Thermal conductivity. The thermal conductivities at all temperatures decrease with the field, and almost turn flat at 2 T because of the field suppression of the electronic thermal conductivity. (f) zT. A peak zT = 2.6 is achieved at 100 K, 0.4 T, because of the positive magneto-Seebeck, as well as negative magnetoresistance and magnetothermal conductivity.

below 1.2 T are plotted as functions of $1/B$ in the embedded figure. Analysis of $\Delta\rho$ *vs.* $1/B$ gives a period of 1.5 T^{-1} related to the Fermi surface area (S_F) by $S_F = \frac{2\pi e}{\hbar}\left(\Delta\frac{1}{B}\right)^{-1}$, which gives $S_F = 6.35 \times 10^{11}$ cm^{-2}. The resolved Fermi surface pockets are HBX pockets, which, in elemental Bi, have an area $S_F = 2.37 \times 10^{12}$ cm^{-2}. The S_F of the 10-ppm doped $Bi_{88}Sb_{12}$ crystal is 27% of the S_F of Bi because of a smaller carrier concentration. The resolved carrier concentration n of the doped crystal is approximately 4.2×10^{16} cm^{-3}, much lower than n_H, because of the Fermi surface anisotropy.[23] The n from SdH oscillations will be used exclusively here for modeling in the theoretical part. The higher-temperature in-field ρ (B) is shown in Fig. 2(b). Weak SdH oscillations can be resolved up to 100 K because of the ultra-small effective mass of the electrons.[17] The negative MR observed at $T < 100$ K is the remnant of the SdH oscillations. Phonon scattering is then decreased by decreasing the phase space for the scattered electrons from 3-D to 1-D. A positive bipolar appears in all fields above 100 K again because of minority carrier excitation.

Fig. 2(c) shows the field dependence of the Seebeck coefficient $S(B)$ at various temperatures, clearly displaying SdH oscillations at 20 and 50 K and remnants at 100 K, which we will model in the next section. At $T \leq 100$ K, $|S|$ slightly increases with the field below 0.1 to 0.5 T, and then remains high up to 1 T. The low-field increase in $|S|$ and decrease in ρ are associated with the transition from a 3-D to a 1-D LL system, when the system transitions from a scattering-limited resistivity at zero field to a largely LL-confined quasi 1-D system with $\mu B \gg 1$. Because of the minimum in ρ and maximum in $|S|$, the power factor S^2/ρ is maximized at low field below 100 K, as shown in Fig. 2(d). The highest power factor is achieved at 80 K, with a magnitude of over 60 mW m^{-1} K^{-2}. Fig. 2(e) shows the field-dependent thermal conductivity results. At all temperatures, κ is already nearly as low as in many classical thermoelectric alloys at zero field because alloy scattering limits the lattice contribution. The field further depresses κ due to the suppression of the electronic contribution. Although the lattice contribution is dominant at low temperatures, the electronic contributions become significant at 50 K and ambipolar one above 100 K; the magnetic field can suppress the latter two and increase zT. Interestingly, both ρ and κ decrease with the field, which seems a violation of the Wiedemann–Franz law ($k_e = LT\sigma$) if L is assumed to be its free electron value. We propose that the magnetic field strongly affects the Lorenz ratio L because the electron–phonon interaction is affected by the magnetic field following the same phase space argument used to explain the negative MR. As a non-magnetic material, the lattice thermal conductivity is not expected to be affected by the magnetic field. An early study showed that the Wiedemann–Franz law is obeyed at zero field with this assumption.[24]

The zT of the 10-ppm doped $Bi_{88}Sb_{12}$ single crystal at various temperatures and fields are calculated from the S, ρ, and κ, obtaining a remarkable value of zT of 2.6 at 100 K, 0.4 T,

which is approximately five times higher than the zero-field value. Thermally excited carriers gradually reduce the overall $|S|$ above 100 K, and the peak zT decreases. At 180 K, a zT of 2 is maintained at 1 T, which is the highest practical field achievable with permanent magnets; therefore, it is still practical for thermoelectric cooling applications.

Temperature-dependent thermoelectric transport properties

To better illustrate the figure of merit change with temperature, we replot the temperature-dependent transport properties at various set fields from 0 to 1.5 T, as shown in Fig. 3. Fig. 3(a) shows $\rho(T)$ with the field. At 0 T, ρ increases monotonically with temperature following a doped semiconductor behavior. The lowest ρ is achieved at a finite field (from 0.1 to 0.5 T), as explained above. When the magnetic field is above 1 T, a sharp increase in ρ is observed with a decreasing temperature, which is harmful for a high zT. $|S|$ also changes non-monotonically with T (Fig. 3(b)). $|S|$ is the maximum when a few LLs are filled, between 0.1 and 1.5 T, and zT is the maximum in the field range where $|S|$ is maximized and ρ is small. Fig. 3(c) shows the temperature-dependent power factors under different magnetic fields. From 0.3 T to 0.7 T, the power factor peaks at 80 K, right before the thermal excitation starts. In this range, the quantum mechanical enhancement of the Seebeck coefficient dominates the increase in the power factor. Above 1 T, the power factor reaches its maximum between 160 K and 180 K, when the classic magneto-Seebeck effect becomes crucial. Fig. 3(d) shows the temperature-dependent κ. κ decreases monotonically with applied field due to the suppression of the electronic or ambipolar contribution. The thermal excitation above 100 K can simultaneously reduce the Seebeck coefficient and elevate the thermal conductivity, as shown in Fig. 3(b) and (d), irrespective of the magnetic field. Therefore, the best zT is observed at 100 K, when a high $|S|$ and low ρ and κ are achieved simultaneously at approximately 0.3–0.4 T, as illustrated in Fig. 3(e).

The high performance of the present Te-doped $Bi_{88}Sb_{12}$ is remarkable, which is not only higher than those reported for undoped samples in the literature,[7,22,25] but also comparable to the high zT values obtained for the best high-temperature materials, as illustrated in Fig. 4(e).[26–31] Such a strong magneto-Seebeck effect and significantly enhanced magneto-zT, together with our previous result in undoped $Bi_{88}Sb_{12}$,[8] and other topological systems like Cd_3As_2,[32–36] highlight the great potential of magneto-thermoelectrics in topological materials for revolutionizing thermoelectric performance. The present work, wherein LL quantization and a quasi-1-D transport regime is realized in optimally doped $Bi_{88}Sb_{12}$ to reach a $zT > 2.5$ below 300 K, opens new avenues for high-performance thermoelectric materials' design and thermoelectric cooling applications.

Theory of Landau quantization enhanced Seebeck coefficient

To prove that the enhancement of $|S|$ in the 0.1 to 1 T range is due to LL quantization, we use the simple model reported by Skinner and Fu,[21] valid when $\mu B \gg 1$ in $Bi_{88}Sb_{12}$ with

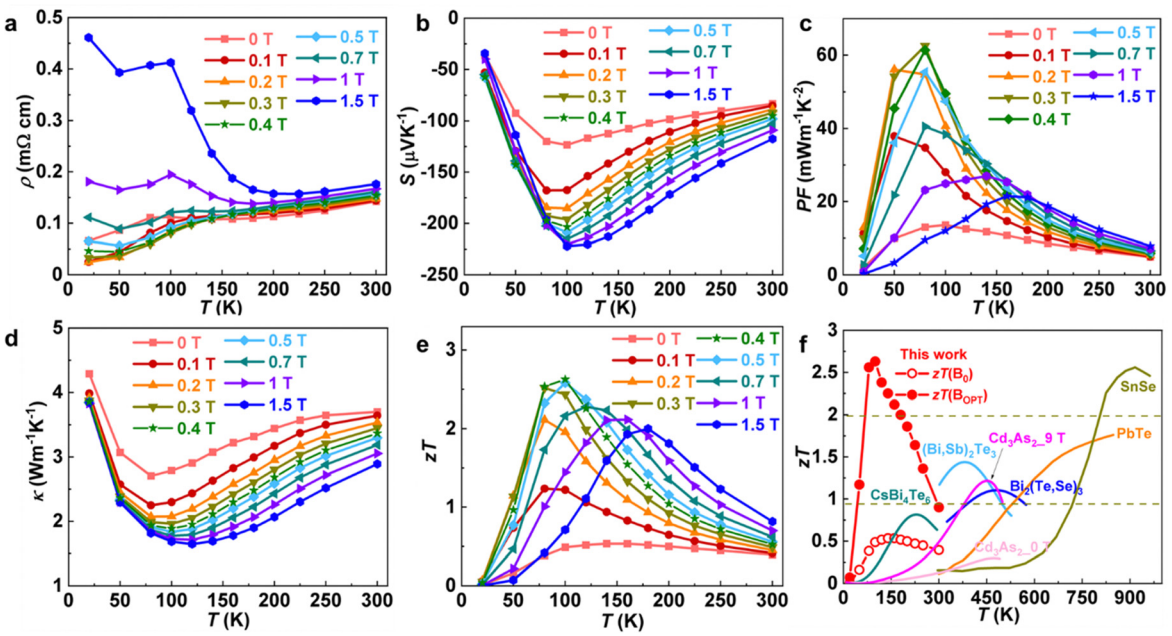

Fig. 3 Temperature-dependent thermoelectric transport properties. The resistivity, Seebeck coefficient, power factor, thermal conductivity, and figure of merit zT at various applied fields are illustrated in (a)–(e), respectively. Below 100 K, a non-monotonic change is observed in the resistivity and Seebeck coefficient measurements because of the SdH oscillations, whereas the thermal conductivity decreases with temperature and the applied field. Above 100 K, the 10-ppm Te-doped crystal behaves close to the undoped $Bi_{88}Sb_{12}$ because the thermally excited carrier starts to dominate the transport properties. The best zT of 2.6 is achieved at 100 K, and in a wide range of temperatures, from 80 to 160 K, a $zT > 2$ can be expected. (f) Comparison between the Te-doped $Bi_{88}Sb_{12}$ and the other high-temperature thermoelectric materials. The current zT is higher than that of most thermoelectric materials, showing the significance of the quantum effect in the low-temperature thermoelectric research.

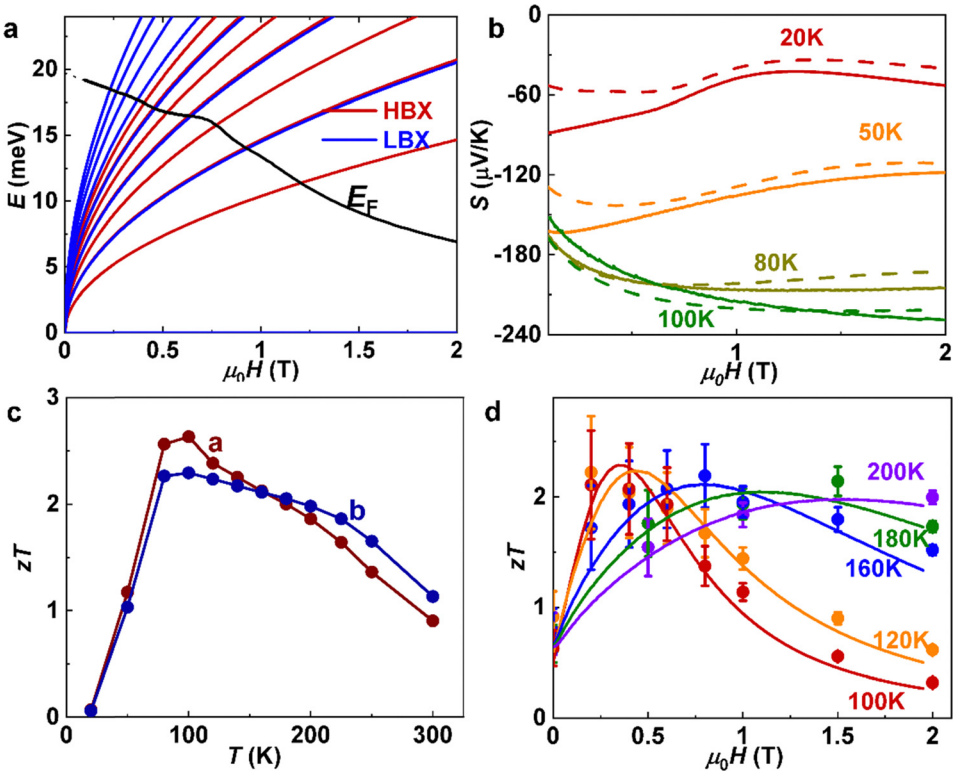

Fig. 4 Theory analysis and reproducibility. (a) The Landau fan diagram of the 10-ppm Te-doped $Bi_{88}Sb_{12}$. Based on the band parameters of $Bi_{88}Sb_{12}$, the fan diagram of the LBX and HBX are plotted separately in red and blue. The Fermi energy is calculated from a carrier concentration of 4.2×10^{16} cm^{-3}. The system should enter the quantum limit at 1.2 T, which is consistent with the experimental transport data. (b) Comparison between the theoretical and experimental in-field Seebeck coefficient modeled at different temperatures and fields. Solid lines are theoretical predictions, and the dashed lines are experimental values. (c) Reproducibility of the high zT. A second crystal b is measured, with a result close to that of the original crystal a. A peak zT of 2.3 is achieved, along with a wider range of $zT > 2$ from 80 to 200 K. (d) Field dependent zT of b at selected temperatures, resolved from the zT calculation (solid lines) and Harman test (full circles). The raw curves of the Harman test are shown in Fig. S10 (ESI†).

Dirac band dispersion. The carrier concentration was taken as $n = 4.2 \times 10^{16}$ cm^{-3}, which was obtained from the SdH frequency. Noting that the band structure of $Bi_{88}Sb_{12}$ is almost exactly the mirror image of that of elemental Bi, except for the absence of T-point holes and the inversion of the symmetric and antisymmetric bands at the L-point of the BZ, we used the detailed LL diagram and effective masses published for the LBX and HBX Bi L-point electrons shown in Fig. 4(a).[18] The calculated Seebeck coefficient is shown in Fig. 4(b). The calculations reproduced the measured field and temperature dependence of S almost quantitatively to 100 K, establishing the validity of the model and attributing the large zT to 1-D LL quantization. The slight difference may come from a finite number of minority holes as well as Fermi surface anisotropy.

Reproducibility of the high thermoelectric performance

To illustrate the sample-to-sample reproducibility, we measured a second 10-ppm crystal (denoted as b) and compared it with the first crystal (denoted as a). We discovered that an unintentional slight variation in the carrier concentration resulted in the peak zT of sample b being slightly lower than that of sample a, but the high zT of sample b was achieved over a wider temperature range than that of sample a, which can be observed in Fig. 4(c). Sample b shows a peak zT of 2.3, with $zT > 2$ from 80 to 225 K and improved performance up to 300 K. The transport properties of sample b are shown in Fig. S4 (ESI†). Because the claim of a record zT requires the confirmation of the results using more than one measurement method,[37] we also performed the Harman test on crystal b, as shown in Fig. 4(d). The Harman zT is determined by the ratio between the adiabatic resistivity ρ_a and isothermal resistivity ρ_i, *via* $zT = \rho_a/\rho_I - 1$.[38] The Harman zT is plotted as full circles together with the transport-calculated zT (lines). This agreement proves the reliability of the reported enhancement in zT.

Summary and outlook

In summary, a record zT of 2.6 is obtained at 100 K and 0.4 T in the 10-ppm Te-doped $Bi_{88}Sb_{12}$ single crystal, which is attributed to the LL quantization enhancement. The 1-D quantization distorts the density of states into the δ-shaped energy distribution of the density-of-states and enhances the figure of merit. This approach not only produces the high zT at cryogenic temperatures on par with the best high-temperature thermoelectric materials but also opens a new venue of research for thermoelectric cooling based on the topological materials with

high magnetic field tunability. Furthermore, we highlight that precise ppm-level doping is essential for realizing the LL quantization by pushing the Fermi energy into the optimal level in the conduction band of the $Bi_{88}Sb_{12}$ topological insulator. This can be instructive for future studies in but not limited to the $Bi_{1-x}Sb_x$ system. Most importantly, we expect more studies using LL quantization to greatly enhance the thermoelectric performance in topological materials, providing a wide material platform for thermoelectric cooling applications and thermal management in the future.

Methods

1. Crystal growth

The single-crystal $Bi_{88}Sb_{12}$ is grown using a traveling molten zone method.[38] To achieve high-quality crystals, 99.9999% Bi is essential, and it was purified by zone melting before use. 6N Bi, Sb, and Te from Alfa Aesar are used in this study. For the doped samples, a piece of Bi containing 0.1% Te was prepared first and then further diluted to the desired Te concentration. For the $Bi_{88}Sb_{12}$ alloy, the seed and feed were prepared separately following the phase diagram. The use of the seed-feed method can minimize the super cooling effect. Pure Bi, Sb, and 0.1% Te-doped Bi were weighed by stoichiometry and loaded into quartz ampoules. The ampoules were sealed under vacuum of 3×10^{-3} mbar and loaded into a box furnace. Polycrystals were first prepared by melting the seed and feed at 700 °C, with frequent shaking of the ampoules for composition homogeneity. The ampoules were quenched to room temperature to minimize the phase segregation introduced by the super cooling procedure. In this study the seed and feed are selected as $Bi_{96}Sb_4$ and $Bi_{88}Sb_{12}$. The obtained seed and feed were cut to have flat ends, physically attached next to each other, and resealed in a second quartz ampoule for further single-crystal growth. A home built horizontal zone melting furnace is used for the crystal growth, and the growing process started at a speed of 1 mm per hour. The as-grown crystals were cleavable with the cleavage plane perpendicular to the trigonal axis.

2. Crystal characterization

Powder diffraction was obtained using the X-ray Guinier technique (Huber G670 with Cu K_α radiation). Single-crystal Laue diffraction analysis was performed using a Bruker single-crystal diffractometer. The chemical composition of the sample was determined by point and area measurements using EDX (energy dispersive X-ray) spectroscopy in a scanning electron microscope (JSM 7800F, Jeol). At an excitation voltage of 10 kV and a beam current of 630 pA, the spectra were recorded with a silicon drift detector (SDD) (Quanta 400 EDX system, Bruker-Nano). The element concentrations were calculated from the intensities of the Bi M and Sb L lines using the matrix correction model eZAF (Benchmark EDS-analytical software). A series of sample characterization, including optical imaging, XRD, and SEM, are shown in ESI,† Fig. S6–S8. A cross-sectional lamella for scanning transmission electron microscopy (STEM) analysis was obtained using a standard focused ion beam (FIB) lift-out procedure with a Thermo Fisher Scientific Helios NanoLab G3 CX FIB. The STEM images were collected in a high-angle annular dark-field (HAADF) configuration on a double-aberration-corrected JEOL ARM300F instrument operating at 300 kV with a probe convergence semi-angle of 30 mrad. The STEM images are shown in Fig. S9 (ESI†).

3. Transport property measurements

All transport measurements were performed using a Quantum Design Physics Property Measurement System (PPMS). The electrical transport (resistivity and Hall) was measured using the built-in electrical transport option (ETO) of the PPMS. The thermal/thermoelectric transport was measured using a one-heater, two-probe steady-state method with a breakout box. The precision voltages were measured using Keithley 2181A nanovoltmeters. In this set of experiments, we used a type-E thermocouple for thermometry, with no obvious field dependence expected down to 20 K. All field-dependent data were interpolated for zT calculation. As the resistivity and thermal conductivity were measured using the same mount, the geometrical uncertainty was limited to 15%, but it still was the dominant factor.

Throughout the study, the field was parallel to the bisectrix direction (010), and an electrical/heat current was applied along the trigonal direction (001). The sign convention follows the Gerlach convention of transport coefficients, where a negative Hall slope indicates that electrons are the majority carriers.

4. Harman test of the figure of merit

The Harman[39] test was performed *in situ* on the transport sample. We performed a DC resistance measurement under a current pulse, first reading the voltage V_i immediately after the pulse was applied when the sample was still at a constant temperature. Under the current, the sample developed a temperature gradient owing to the Peltier effect; the voltage V_a was read after the gradient reached a steady state. The Harman zT was then $zT = V_a/V_i - 1$. A Keithley 6220 current source was used for the DC current supply, and a Keithley nano-Voltmeter 2182A was used for the voltage measurement. A current of 10 mA was applied to the sample and the voltage was recorded simultaneously. A total of 200–300 time-step points were recorded until the voltage reached a steady state. LabVIEW software was used for measurement control to collect a precise isothermal voltage V_i and the time evolution of the voltage until the adiabatic value of V_a. The raw curves of the Harman test are shown in Fig. S10 (ESI†).

5. Theory and calculations

To account for the thermopower of $Bi_{88}Sb_{12}$ under magnetic fields close to the quantum limit, the system was treated in the Landau level regime. Electrons from the pockets at the L points in $Bi_{88}Sb_{12}$ were described as Dirac fermions. The Landau level diagram was then calculated as

$$\varepsilon_{kl} = \mathrm{sign}(l)\sqrt{\frac{2\hbar^2 v^2}{l_B{}^2}|l| + \hbar^2 v^2 k^2}$$

The average Fermi velocity v was assumed as 4×10^5 m s^{-1}, and l is the Landau level index. The Fermi level is determined from n as follows. The density of states is $eBk/(4\pi^2\hbar)$ on each level. For a given value of E_F and the LL diagram at each field, the Fermi wavevector $k_{F,j}$ on each level can be derived. The sum over all levels of $eBk_{F,i}/(4\pi^2\hbar)$ gives the carrier concentration in degenerate statistics; setting this equal to n gives the value of E_F at each field, also plotted in Fig. 4(a). The Seebeck coefficient of the Landau level system was calculated based on the model reported by Skinner and Fu.[21]

$$S = -\frac{k_B}{e}\frac{N_v}{\pi n l_B^2}\frac{1}{2\pi}\int_{-\infty}^{\infty}\frac{dk}{2\pi}\sum_{l=-\infty}^{\infty}[f\ln f + (1-f)\ln(1-f)]$$

where k_B is the Boltzmann constant, e is the elemental charge, n is the carrier concentration, l_B is the magnetic length, and $(l_B^2 = \frac{\hbar}{eB})$, f is the Fermi Dirac distribution $(f(\varepsilon) = \{1 + \exp[(\varepsilon - E_F)/k_BT]\}^{-1})$. N_v is the degeneracy of the Fermi surface pockets. To account for the LBX and HBX in this anisotropic system, here we assign N_v to be 1 for LBX and 2 for HBX with the spin degeneracy lifted under magnetic fields. The Fermi level E_F was determined by the carrier concentration $n = 4.2 \times 10^{16}$ cm^{-3}, obtained by solving the quantum oscillation. As the magnetic field intensity increases, the Fermi level decreases as the density of states increases. When the magnetic field is sufficiently large, the system enters the extreme quantum limit with only the zeroth Landau level left, resulting in a non-saturating Seebeck coefficient at low temperatures.

6. Uncertainty analysis

In the transport measurement, the uncertainty in the Seebeck measurement, which is of the order of 5%, comes from the uniformity of the sample. In the temperature range of interest, particularly from 80 to 200 K, the field dependence of the thermocouple sensitivity is below 2% and is neglected. For the resistivity and thermal conductivity, the uncertainty mainly originates from the geometrical uncertainty, particularly the size of the longitudinal contacts. The magnitudes of the uncertainty in κ and ρ were estimated to be 5% each, but this geometric uncertainty was canceled out in the zT calculation. We found a 3% change in the heater resistance when it was cooled from 300 to 20 K. Additionally, a 1–3% temperature uncertainty was generated when the temperature gradient is applied to the sample. As a result, the total uncertainty in the zT calculation is estimated as $10\% \pm 1\%$.

The uncertainty in the Harman method is due to the difficulty of precisely determining the initial voltage V_i. This uncertainty is larger at a low field, where it can reach 25% at 100 K. With an increasing field, this error turns smaller, with a magnitude of 10% at 1 T and 3% at 2 T. The uncertainty of the Harman method is represented by the error bars shown in Fig. 4(d).

Author contributions

B. H. and Y. P. designed this work, grew the single crystals, and performed the characterization. B. H. performed the transport measurements; B. H. and F. M. S. conducted the Harman test; U. B. performed the SEM-EDX analysis; B. H. G. performed the STEM imaging. B. H., Y. P., D. C., M. N., H. H., J. P. H., and C. F. analyzed the data; and the theoretical model was built by X. F. and J. P. H.; C. F. supervised the project. All authors were involved in writing the paper.

Data availability

All datasets generated or analyzed during this study are available from the corresponding author upon reasonable request.

Conflicts of interest

The authors declare no competing interests.

Acknowledgements

This work was financially supported by the Deutsche Forschungsgemeinschaft (DFG) under SFB1143 (project no. 247310070) and the Würzburg-Dresden Cluster of Excellence on Complexity and Topology in Quantum Matter-ct.qmat (EXC 2147, project no. 390858490). Y. P. acknowledges the financial support from the National Natural Science Foundation of China (grant no. 52401263). J. P. Heremans received support from the MRSEC program of the U.S. National Science Foundation (NSF), grant number DMR 2011876. B. H. G. was supported by Schmidt Science Fellows, in partnership with the Rhodes Trust. Open Access funding provided by the Max Planck Society.

References

1 L. E. Bell, *Science*, 2008, **12**, 1457–1461.
2 L. D. Hicks and M. S. Dresselhaus, *Phys. Rev. B: Condens. Matter Mater. Phys.*, 1993, **47**, 16631(R).
3 J. P. Heremans, V. Jovovic, E. S. Toberer, A. Saramat, K. Kurosaki, A. Charoenphakdee, S. Yamanaka and G. J. Snyder, *Science*, 2008, **321**, 5888.
4 D. Hsieh, D. Qian, L. Wray, Y. Xia, Y. S. Hor, R. J. Cava and M. Z. Hasan, *Nature*, 2008, **452**, 970–974.
5 Y. Pan, B. He, X. Feng, F. Li, D. Chen, U. Burkhardt and C. Felser, *Nat. Mater.*, 2025, **24**, 76–82.
6 G. J. Snyder and E. S. Toberer, *Nat. Mater.*, 2008, **7**, 105–114.
7 J. He and T. M. Tritt, *Science*, 2017, **357**, eaak9997.
8 R. Wolfe and G. E. Smith, *Appl. Phys. Lett.*, 1962, **1**, 5–7.
9 J. Mao, G. Chen and Z. Ren, *Nat. Mater.*, 2020, **20**, 454–461.
10 M. Cutler and N. F. Mott, *Phys. Rev.*, 1969, **181**, 1336.
11 G. D. Mahan and J. O. Sofo, *Proc. Natl. Acad. Sci. U. S. A.*, 1996, **93**, 7436–7439.
12 J. P. Heremans, C. M. Thrush, D. T. Morelli and M.-C. Wu, *Phys. Rev. Lett.*, 2002, **88**, 216801.

13 A. I. Hochbaum, R. Chen, R. D. Delgado, W. Liang, E. C. Garnett, M. Najarian, A. Majumdar and P. Yang, *Nature*, 2008, **461**, 163–168.
14 L. Schubnikow and W. De Haas, *Nature*, 1930, **126**, 500.
15 R. Hartman, *Phys. Rev.*, 1969, **181**, 1070.
16 R. D. Brown, R. L. Hartman and S. H. Koenig, *Phys. Rev.*, 1968, **172**, 598–603.
17 D. Shoenberg, *Magnetic Oscillations in Metals*. Cambridge University Press, 1984.
18 M. P. Vecchi, J. R. Pereira and M. D. Dresselhaus, *Phys. Rev. B*, 1976, **14**, 298–316.
19 G. E. Smith and R. Wolfe, *J. Appl. Phys.*, 1962, **33**, 841–846.
20 H. J. Goldsmid, *Phys. Status Solidi A*, 1970, **1**, 7–28.
21 B. Skinner and L. Fu, *Sci. Adv.*, 2018, **4**, eaat 2621.
22 W. M. Yim and A. Amith, *Solid-State Electron.*, 1972, **15**, 1141–1144.
23 E. H. Putley, *The Hall Effect and Relate Phenomena*, Butterworth & Co. Limited, 1960.
24 C. Uher and H. J. Goldsmid, *Phys. Status Solidi B*, 1974, **65**, 765.
25 V. M. Grabov and O. N. Uryupin, Proc. 16th Int Conf Thermoelectrics, 1997, 176–179.
26 B. Poudel, Q. Hao, Y. Ma, Y. Lan, A. Minnich, B. Yu, X. Yan, D. Wang, A. Muto, D. Vashaee, X. Chen, J. Liu, M. S. Dresselhaus, G. Chen and Z. Ren, *Science*, 2008, **320**, 634–638.
27 Y. Pan and J.-F. Li, *NPG Asia Mater.*, 2016, **8**, e275.
28 Y. Pei, X. Shi, A. LaLonde, H. Wang, L. Chen and G. J. Snyder, *Nature*, 2011, **473**, 66–69.
29 D.-Y. Chung, T. Hogan, P. Brazis, M. Rocci-Lane, C. Kannewurf, M. Bastea, C. Uher and M. G. Kanatzidis, *Science*, 2000, **287**, 1024–1027.
30 L.-D. Zhao, S.-H. Lo, Y. Zhang, H. Sun, G. Tan, C. Uher, C. Wolverton, V. P. Dravid and M. G. Kanatzidis, *Nature*, 2014, **508**, 373–377.
31 H. Wang, X. Luo, K. Peng, Z. Sun, M. Shi, D. Ma, N. Wang, T. Wu, J. Ying, Z. Wang and X. Chen, *Adv. Funct. Mater.*, 2019, **29**, 1902437.
32 W. Zhang, P. Wang, B. Skinner, R. Bi, V. Kozii, C.-W. Cho, R. Zhong, J. Schneeloch, D. Yu, G. Gu, L. Fu, X. Wu and L. Zhang, *Nat. Commun.*, 2020, **11**, 1046.
33 F. Han, N. Andrejevic, T. Nguyen, V. Kozii, Q. T. Nguyen, T. Hogan, Z. Ding, R. Pablo-Pedro, S. Parjan, B. Skinner, A. Alatas, E. Alp, S. Chi, J. Fernandez-Baca, S. Huang, L. Fu and M. Li, *Nat. Commun.*, 2020, **11**, 6167.
34 T. Liang, Q. Gibson, J. Xiong, M. Hirschberger, S. P. Koduvayur, R. J. Cava and N. P. Ong, *Nat. Commun.*, 2013, **4**, 2696.
35 X. Xu, Y. Liu, G. Seyfarth, A. Pourret, W. Ma, H. Zhou, G. Wang, Z. Qu and S. Jia, *Phys. Rev. B*, 2021, **104**, 115164.
36 W. Ouyang, A. C. Lygo, Y. Chen, H. Zheng, D. Vu, B. L. Wooten, X. Liang, J. P. Heremans, S. Stemmer and B. Liao, *Adv. Mater.*, 2024, **36**, 2311644.
37 J. P. Heremans and J. Martin, *Nat. Mater.*, 2024, **23**, 18–19.
38 D. Vu, W. Zhang, C. Şahin, M. E. Flatté, N. Trivedi and J. P. Heremans, *Nat. Mater.*, 2021, **20**, 1525–1531.
39 T. C. Harman, *J. Appl. Phys.*, 1958, **29**, 1373–1374.

